# Multireference quantum chemistry protocol for simulating autoionization spectra: Test of ionization continuum models for the neon atom

Gilbert Grell, Oliver Kühn, and Sergey I. Bokarev[*]

*Institut für Physik, Universität Rostock, Albert-Einstein-Strasse 23-24, 18059 Rostock, Germany*

In this paper we present a protocol to evaluate partial and total Auger decay rates combining the restricted active space self-consistent field electronic structure method for the bound part of the spectrum and numerically obtained continuum orbitals in the single-channel scattering theory framework. Additionally, the two-step picture is employed to evaluate the partial rates. The performance of the method is exemplified for the prototypical Auger decay of the neon $1s^{-1}3p$ resonance. Different approximations to obtain the continuum orbitals, the partial rate matrix elements, and the electronic structure of the bound part are tested against theoretical and experimental reference data. It is demonstrated that the partial and total rates are most sensitive to the accuracy of the continuum orbitals. For instance, it is necessary to account for the direct Coulomb potential of the ion for the determination of the continuum wave functions. The Auger energies can be reproduced quite well already with a rather small active space. Finally, perspectives of the application of the proposed protocol to molecular systems are discussed.

## I. INTRODUCTION

Ionization triggered by photon absorption occurs along two pathways. In direct photoionization, the energy is transferred to an ejected electron. Alternatively, the system can be first put into a metastable state by a resonant excitation and afterwards decay via an autoionization mechanism. Autoionization can be approximately understood as a two-step process [1], in which the decay can be considered independently from the excitation process and interferences between direct and autoionization are neglected. For example, let us consider an atomic species, such as a neon atom that is prepared in a highly excited state $|\Psi_i\rangle$ above the continuum threshold at $E = 0$ eV (Fig. 1). This state spontaneously decays into the continuum state $|\Psi_\alpha\rangle$ consisting of the discrete state $|\Psi_f^+\rangle$ of the ion and the emitted electron, $|\psi_\alpha\rangle$, carrying the excess energy $\varepsilon_\alpha = \mathcal{E}_i - \mathcal{E}_f$. The system's electronic structure is thus encoded into the kinetic-energy spectrum of the ionized electrons. Photoelectron spectroscopy (PES) and autoionization spectroscopy (AIS) map bound states to the continuum, which makes them less sensitive to selection rule suppression and more informative than spectroscopies involving optical transitions between bound states [2–4].

Autoionization processes, predominantly Auger decay [5] but also interatomic Coulombic decay (ICD) [6] and electron transfer mediated decay (ETMD) [7], are particularly interesting on their own. Due to their correlated nature, they not only probe but also initiate or compete with intricate ultrafast electronic and nuclear dynamics (see, e.g., [8–12]). Additionally, they provide the main channel for the decay of core vacancies [13] and play a key role in biological radiation damage, creating highly charged cations while a cascade of highly reactive low-energy electrons is emitted [11,14–17]. Further, in free-electron laser experiments operating with ultrashort intense x-ray pulses, autoionization after multiple photoionization induces the Coulomb explosion of the target, which limits the achievable spectroscopic and temporal resolution [18]. Due to this wealth of applications, autoionization and especially the local Auger effect have been studied extensively both theoretically and experimentally since their discovery by Meitner [5] and description by Wentzel [1].

Remarkably, AIS simulations of molecular systems remain challenging today, although the fundamental theory has been known for decades [19–21]. For atoms, methods combining highly accurate four-component multiconfigurational Dirac-Fock (MCDF) calculations with multichannel scattering theory are publicly available [22], whereas no such general purpose code exists for molecules. The main complication of the molecular case lies in the construction of molecular continuum states $|\Psi_\alpha\rangle$. The approaches to the simulation of AIS published during the last decades can be classified into two families—those that circumvent the continuum orbital problem and those that treat the continuum orbital explicitly.

The first family consists of the following approaches. The simplest method that allows one to assign experimental AIS is to evaluate the energetic peak positions [23–25]. Additionally, simple estimates for the partial decay rates can be obtained based on an electron population analysis [26]. More advanced approaches rely on an implicit continuum representation with Stieltjes imaging [27], a Green's-function operator [28,29], or a propagator formalism [30,31]. From this group, the Fano-Stieltjes algebraic diagrammatic construction (Fano-ADC) method [32] has been used to evaluate Auger, ICD, and ETMD decay rates of van der Waals clusters [33], first row hydrides [34], and the $[\mathrm{Mg(H_2O)_6}]^{2+}$ cluster [11].
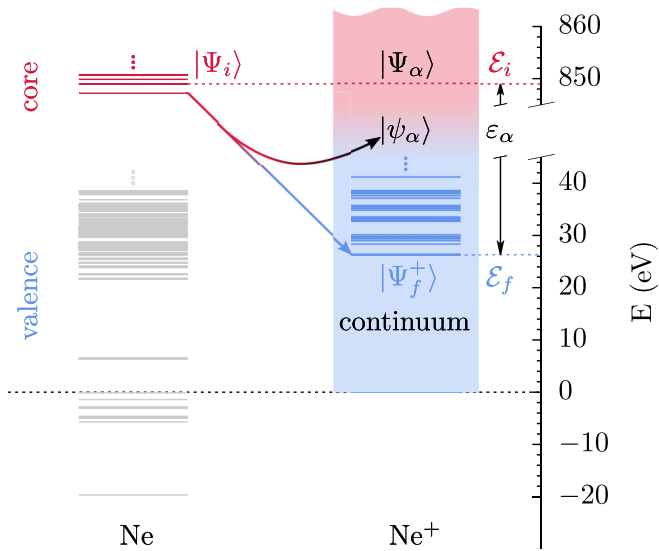
_____
*sergey.bokarev@uni-rostock.de

FIG. 1. Autoionization scheme for the neon atom. The core vacancy state $|\Psi_i\rangle$ with energy $\mathcal{E}_i$ (red/dark gray) decays isoenergetically into the continuum state $|\Psi_\alpha\rangle$ (black) composed of the ionic bound state $|\Psi_f^+\rangle$ with energy $\mathcal{E}_f$ (blue/gray) and the continuum orbital $|\psi_\alpha\rangle$ of the outgoing electron with the excess energy $\varepsilon_\alpha$. States that do not contribute to the process are depicted in light gray; the singly ionized continuum is denoted by the color gradient/shaded area.

Therein, the continuum is approximately represented with spatially confined basis functions. However, the description of Auger electrons with kinetic energies of several hundred electronvolts requires large basis sets leading to computationally demanding simulations.

The second family, relying on an explicit representation of the continuum wave function, consists of the following approaches. The one-center approximation uses atomic continuum functions centered at the vacancy-bearing atom to describe the outgoing electron in the evaluation of partial decay rates [35–38]. This approximation can be applied on top of high-level electronic structure methods [39]. It is also applied in the XMOLECULE package [40,41], which is based on very cost efficient electronic structure calculations and atomic continuum functions. This allows for the evaluation of ionization cascades but may limit the applicability for strongly correlated systems, e.g., systems possessing a multiconfigurational character. Further, the influence of the molecular field may be taken into account perturbatively [42,43] or in a complete manner with, e.g., the single-center approach, where the whole molecular problem is projected onto a single-centered basis [44–49].

Finally, multichannel scattering theory methods that combine finite multicentered basis sets with the appropriate boundary conditions to represent the molecular continuum have been developed [50] and applied to the AIS of a variety of small systems [50–52]. For instance, the recently developed XCHEM approach [53] has been applied to simulate PES and AIS of atoms [54] and small molecular systems [55]. These techniques represent the most general and accurate quantum-mechanical treatment of the problem, thus potentially serving

as a high-level reference, although connected to substantial computational effort.

Summarizing, most of the above-mentioned methods have been applied only to simple diatomics, first row hydrides, halogen hydrides, and small molecules consisting of not more than two heavy atoms. Studies of larger molecular systems, such as tetrahedral molecules, small aldehydes, and amides [56,57]; solvated metal ions [11]; and polymers [58] are very scarce. In fact, the FANO-ADC [32,33] and the XMOLECULE [40,41] approaches are the only publicly available tools that allow one to simulate AIS for a variety of systems without restricting the molecular geometry. Further, both methods are not suited to treat systems possessing multiconfigurational wave functions. This puts studies of some chemically interesting systems having near degeneracies, e.g., transition-metal compounds, or of photodynamics in the excited electronic states, e.g., near conical intersections, out of reach. To keep up with the experimental advancements, the development of a general purpose framework to evaluate autoionization decay rates (Auger, ICD, and ETMD) for molecular systems is warranted. Such a framework should be kept accessible, transferable, and easy to use; i.e., it should be based on widespread robust and versatile quantum chemistry (QC) methods.

Here, we present a protocol that combines multiconfigurational restricted active space (RAS) self-consistent field (SCF) (RASSCF) bound-state wave functions with single-centered numerical continuum orbitals in the single-channel scattering theory framework [59]. We have chosen the RASSCF approach since it is known to yield reliable results for core-excited states [60], needed in the simulation of x-ray absorption [61,62], resonant inelastic scattering [63,64], and photoemission spectra [65–67], suggesting its application to AIS.

Although the ultimate goal is to investigate molecules, this proof-of-concept paper focuses on the simulation of the prototypical neon $1s^{-1}3p$ Auger electron spectrum (AES) to calibrate the approach, since highly accurate reference data are available from both theory [68] and experiment [69–72]. Special attention is paid to the representation of the radial continuum waves, which is investigated herein by a thorough test of different approximations. Note that our implementation allows one to calculate molecular AIS as well as PES, which will be presented elsewhere.

We commence this paper with an introduction to the underlying theory and further give important details of our implementation. The paper continues with the computational details and the benchmark of our results against theoretical and experimental references. Finally, we conclude the discussion and present perspectives for the molecular application.

## II. THEORY

The approach for the calculation of partial autoionization rates consists of the following approximations.

(1) The two-step model [1] is employed; i.e., excitation and decay processes are assumed to be decoupled and interference effects between photoionization and autoionization are neglected (Fig. 1). Within this approximation, the partial

autoionization rate for the decay $i \to \alpha$ reads [19]

$$\Gamma_{i\alpha} = 2\pi |\langle \Psi_\alpha | \mathcal{H} - \mathcal{E}_i | \Psi_i \rangle|^2. \qquad (1)$$

Atomic units are used throughout, unless explicitly stated otherwise.

(2) We require that all bound-state wave functions have the form of configuration interaction (CI) expansions in terms of $N$-electron Slater determinants:

$$|\Psi\rangle = \sum_j C_j a_{j_1,\sigma_1}^\dagger \cdots a_{j_N,\sigma_N}^\dagger |0\rangle. \qquad (2)$$

The $a_{i,\sigma_i}^\dagger$ are the usual fermionic creation operators in the spin-orbital basis $\{\varphi_{i,\sigma_i}\}$. In this paper, multiconfigurational bound-state wave functions for the unionized and ionized states $|\Psi_i\rangle$ and $|\Psi_f^+\rangle$ are obtained with the RASSCF or restricted active space second-order perturbation theory (RASPT2) method. However, the presented protocol can employ any CI-like QC method.

(3) The limit of weak relativistic effects is assumed; thus, the total spins $S$ and $S^+$ and their projections onto the quantization axis $M$ and $M^+$ of the bound un-ionized and ionized systems are good quantum numbers. Further, $S$ and $M$ are conserved during the autoionization process.

(4) The single-channel scattering theory framework is employed, disregarding interchannel coupling as well as correlation effects between the bound and outgoing electrons.

(5) The continuum orbitals are treated as spherical waves, subject to the spherically averaged potential $V_f(r)$ of the ionic state $|\Psi_f^+\rangle$. Hence, the continuum orbitals have the form

$$\psi_{\alpha,\sigma}(r,\vartheta,\phi) = \frac{1}{r} w_l^{fk}(r) Y_l^m(\vartheta,\phi) \zeta(\sigma), \qquad (3)$$

with spherical harmonics $Y_l^m(\vartheta,\phi)$ being the angular part and $\zeta(\sigma)$ being the spin function. For brevity, $\zeta(\sigma)$ is generally omitted and present only when needed. The composite channel index $\alpha = (f, l, m, k)$ contains the index of the ionized state $f$, the orbital and magnetic quantum numbers $l$ and $m$, and the wave number $k = \sqrt{2\varepsilon_\alpha}$ of the continuum orbital. This notation uniquely identifies the total energy $\mathcal{E}_\alpha = \mathcal{E}_f + \varepsilon_\alpha$ and the continuum orbital and bound state for each channel $|\Psi_\alpha\rangle$. Generally, indices $i$ and $f$ always refer to bound states of the un-ionized and ionized species and $\alpha$ denotes decay channels.

The radial part $w_l^{fk}(r)/r$ is determined by solving the radial Schrödinger equation:

$$\left[ \frac{d^2}{dr^2} + 2\left( \frac{k^2}{2} - V_f(r) \right) - \frac{l(l+1)}{r^2} \right] w_l^{fk}(r) = 0. \qquad (4)$$

With the assumptions 1–5, the $N$-electron ionized continuum states with conserved total spin and projection of the un-ionized states, $S$ and $M$, can be written as

$$|\Psi_\alpha\rangle = \sum_{M^+=-S^+}^{S^+} \sum_{\sigma=-\frac{1}{2},\frac{1}{2}} C_{S^+,M^+;\sigma}^{S,M} |\Upsilon_\alpha^{\sigma M^+}\rangle, \qquad (5)$$

where $\sigma$ is the spin projection of the outgoing electron. The Clebsch-Gordan coefficients $C_{S^+,M^+;\sigma}^{S,M} = \langle S, M | S^+, M^+; \frac{1}{2}, \sigma \rangle$ couple the channel functions $|\Upsilon_\alpha^{\sigma M^+}\rangle$. These are constructed by inserting an additional electron with the continuum orbital

$|\psi_{\alpha,\sigma}\rangle$ into the bound ionic state with spin projection $M^+$, retaining the antisymmetry:

$$|\Upsilon_\alpha^{\sigma M^+}\rangle = a_{\alpha,\sigma}^\dagger |\Psi_{f,M^+}^+\rangle. \qquad (6)$$

Note that in contrast to the continuum state $|\Psi_\alpha\rangle$, which is an eigenstate of $\mathbf{S}^2$ and $S_z$, the $|\Upsilon_\alpha^{\sigma M^+}\rangle$ are not eigenfunctions of $\mathbf{S}^2$, but only of $S_z$.

## III. DETAILS OF THE IMPLEMENTATION

### A. Model potentials

We commence with the discussion of different approximations to the potential $V_f(r)$ in Eq. (4), which are central for the quality of the free-electron function. In this paper, we have used the following models:

$$V^{\text{free}} = 0, \qquad (7a)$$

$$V^{\text{eff}}(r) = -\frac{Z_{\text{eff}}}{r}, \qquad (7b)$$

$$V_f^{\text{scr}}(r) = -\frac{Z_f(r)}{r}, \qquad (7c)$$

$$V_f^{\text{J}}(r) = -\frac{Z}{r} + J_f(r), \qquad (7d)$$

$$V_f^{\text{JX}}(r) = -\frac{Z}{r} + J_f(r) + X_f^{\text{S}}(r). \qquad (7e)$$

In words, we use (a) no potential; (b) an effective Coulomb potential with a fixed charge $Z_{\text{eff}}$; (c) the screened Coulomb potential of an ionic state $f$ with the charge $Z_f(r)$ varying with distance; (d) the nuclear, $-Z/r$, and spherically averaged direct potential of the ionic state, $J_f(r)$; and (e) the potential of approach (d) augmented with Slater's exchange term $X_f^{\text{S}}(r)$ [73]. Details on the definition of $Z_f(r)$, $J_f(r)$, and $X_f^{\text{S}}(r)$ are given in Appendix A.

### B. Continuum orbitals

The solutions to the radial Schrödinger equation, Eq. (4), using the potentials (7a)–(7e) can be understood as follows: In approach (a), assuming a free particle, we completely neglect any influence of the ion onto the outgoing electron. Here, the radial part of $\psi_{\alpha,\sigma}(r,\vartheta,\varphi)$ corresponds to spherical Bessel functions $j_l(kr)$ [74]:

$$\psi_{\alpha,\sigma}^{\text{free}}(r,\vartheta,\phi) = \sqrt{\frac{2}{\pi}} k\, j_l(kr) Y_l^m(\vartheta,\phi) \zeta(\sigma). \qquad (8)$$

The prefactor $\sqrt{\frac{2}{\pi}} k$ ensures the correct normalization,

$$\langle \psi_{\alpha,\sigma} | \psi_{\alpha',\sigma'} \rangle = \delta_{ll'} \delta_{m_l m_l'} \delta_{\sigma\sigma'} \delta(\varepsilon_\alpha - \varepsilon_{\alpha'}), \qquad (9)$$

which is exact only for the free-particle approach, and approximate for all other potentials, due to the long-range Coulomb distortion.

An effective Coulomb form [approach (b)] is the simplest approach to approximately account for the ionic potential. It has the advantage that the solutions to Eq. (4) are still analytically available in the form of regular Coulomb functions

$F_l$ [74]:

$$\psi_{\alpha,\sigma}^{\text{eff}}(r,\vartheta,\phi) = \sqrt{\frac{2}{\pi k}} \frac{F_l(\eta, kr)}{r} Y_l^m(\vartheta,\phi)\zeta(\sigma), \quad (10)$$

with $\eta = -Z_{\text{eff}}/2k$.

Approaches (c)–(e) employ numerically obtained potentials according to Eqs. (7c)–(7e) and thus require a numerical solution of the radial Schrödinger equation (4). It is done using Numerov's method and the numerically obtained radial waves are scaled so as to satisfy the asymptotic boundary conditions:

$$w_l^{fk}(r \to 0) = nr^{l+1}, \quad (11a)$$

$$w_l^{fk}(r \to \infty) = \sqrt{\frac{2}{\pi k}} \big[ \cos \delta_l^f(k) F_l(\eta, kr) \\ + \sin \delta_l^f(k) G_l(\eta, kr) \big]. \quad (11b)$$

The scaling factors and phase shifts $\delta_l^f(k)$ are obtained by matching the numerical solutions and their first derivatives with a linear combination of the regular and irregular Coulomb functions $F_l$ and $G_l$ (see [74]). This matching is carried out in the asymptotic region, where the potential is well approximated by the Coulomb potential of the ions' net charge $V_f(r) \approx -Z_{\text{net}}/r$.

Since the screened Coulomb potential model, Eq. (7c), is an *ad hoc* assumption based on the simple idea that the nuclear charge is screened by the integrated electron density, the applicability of this model needs to be tested. In turn, approaches (d) and (e), employing the spherically averaged direct Coulomb and exchange terms according to Eqs. (7d) and (7e), in a sense correspond to the Hartree and Slater-$X_\alpha$ levels of accuracy, respectively.

The continuum orbitals obtained by any of these methods are not orthogonal to the bound orbitals, which is in contrast to the behavior that an exact continuum orbital would possess.

### C. Continuum matrix elements

Using the decomposition of the continuum states in terms of channel functions in Eq. (5) and separating the Hamiltonian into its one- and two-electron parts $\mathcal{H} = \sum_u h_u + \sum_{u<v} 1/r_{uv}$, the partial decay rate becomes

$$\Gamma_{i\alpha} = 2\pi \left| \sum_{M^+,\sigma} C_{S^+,M^+;\sigma}^{S,M} \left[ \sum_u \langle \Upsilon_\alpha^{\sigma M^+} | h_u | \Psi_i \rangle \right. \right.$$
$$\left. \left. + \sum_{u<v} \langle \Upsilon_\alpha^{\sigma M^+} | \frac{1}{r_{uv}} | \Psi_i \rangle - \mathcal{E}_i \langle \Upsilon_\alpha^{\sigma M^+} | \Psi_i \rangle \right] \right|^2. \quad (12)$$

Here, $u$ and $v$ are electron indices, $h_u$ contains the electronic kinetic-energy and electron-nuclei attraction terms, and $1/r_{uv}$ is the electron repulsion.

The expressions for the overlap and one- and two-electron matrix elements in Eq. (12) are obtained by using Löwdin's-Slater determinant calculus [75]. Here one has to take into account that the un-ionized and ionized bound states are obtained in separate SCF calculations. Consequently, they have different sets of $N_{\text{orb}}$ spin orbitals $\{\varphi_i\}$ and $\{\varphi_i^+\}$ that are not mutually orthogonal. The spin coordinates are implicitly assumed to be assigned as introduced in Eq. (2). Then, the

respective creation and annihilation operators are $a_i^\dagger$, $a_i$ and $(a_i^+)^\dagger$, $a_i^+$.

With this, the overlap integral in Eq. (12) can be rearranged into the overlap of the continuum orbital and the Dyson orbital (DO) $|\Phi_{i\alpha}^{M^+}\rangle$:

$$\langle \Upsilon_\alpha^{\sigma M^+} | \Psi_i \rangle = \langle \psi_{\alpha,\sigma} | \Phi_{i\alpha}^{M^+} \rangle. \quad (13)$$

The DO is generally defined as the $N-1$ particle overlap of the un-ionized and ionized states $|\Psi_i\rangle$ and $|\Psi_{f,M^+}^+\rangle$ that are associated with the channel $\alpha$ and can be expressed in second quantization form as a linear combination of the spin orbitals $\{\varphi_s\}$ of the un-ionized species, with the coefficients $\phi_{\alpha,s}^{M^+}$:

$$|\Phi_{i\alpha}^{M^+}\rangle = \sum_{s=1}^{N_{\text{orb}}} \underbrace{\langle \Psi_{f,M^+}^+ | a_s | \Psi_i \rangle}_{\phi_{\alpha,s}^{M^+}} |\varphi_s\rangle. \quad (14)$$

Staying on this route, the one- and two-electron transition matrix elements in Eq. (12) can be expressed as

$$\sum_u \langle \Upsilon_\alpha^{\sigma M^+} | h_u | \Psi_i \rangle = \langle \psi_{\alpha,\sigma} | h | \Phi_{i\alpha}^{M^+} \rangle + \langle \psi_{\alpha,\sigma} | \tilde{\Phi}_{i\alpha}^{1,M^+} \rangle \quad (15)$$

and

$$\sum_{u<v} \langle \Upsilon_\alpha^{\sigma M^+} | \frac{1}{r_{uv}} | \Psi_i \rangle = \sum_{q=1}^{N_{\text{orb}}} \langle \psi_{\alpha,\sigma} \varphi_q^+ | \frac{1}{r_{12}} | \Xi_{i\alpha}^{M^+,q} \rangle$$
$$+ \langle \psi_{\alpha,\sigma} | \tilde{\Phi}_{i\alpha}^{2,M^+} \rangle. \quad (16)$$

Here, $|\Xi_{i\alpha}^{M^+,q}\rangle$ is the two-electron reduced transition density

$$|\Xi_{i\alpha}^{M^+,q}\rangle = \sum_{s_1 \neq s_2}^{N_{\text{orb}}} \langle \Psi_{f,M^+}^+ | (\hat{a}_q^+)^\dagger \hat{a}_{s_1} \hat{a}_{s_2} | \Psi_i \rangle | \varphi_{s_1} \varphi_{s_2} \rangle, \quad (17)$$

and $|\tilde{\Phi}_{i\alpha}^{n,M^+}\rangle$ are the one- and two-electron conjugated Dyson orbitals for $n = 1$ and 2, respectively [see Eqs. (B3) and (B4)]. A simpler formulation of the non-orthogonal (NO) terms proposed in [76] is not used herein, because in practice it is not always strictly equivalent to our approach (see Sec. II of Supplemental Material [77] for details).

The strong orthogonality (SO) approximation, i.e., the assumption that the overlaps of the continuum and all un-ionized orbitals are zero, $\langle \psi_{\alpha,\sigma} | \varphi_{i,\sigma_i} \rangle = 0$, implies that the overlap integrals between the continuum and the ordinary and conjugated Dyson orbitals in Eqs. (13), (15), and (16) vanish. Since the evaluation of the conjugate DOs can be quite involved, SO approximation substantially simplifies the computation.

A similar effect is achieved by using the Gram-Schmidt (GS) orthogonalization to project the orbitals of the ionized system out of the continuum functions and enforce $\langle \psi_{\alpha,\sigma}^{\text{GS}} | \varphi_{i,\sigma_i}^+ \rangle = 0$. This approach has been tried before, e.g., in [44], and will be tested herein as well.

In the following, we will use the labels SO, NO, and GS to indicate that the overlap terms in Eqs. (13), (15), and (16) have been neglected (SO) or fully included (NO) and that GS orthogonalized continuum functions have been used to evaluate the partial rates including the NO terms as well. Further, we also compare the results of the "full" Hamiltonian

TABLE I. QC setups and number of states used in the state-averaged RASSCF calculations.

| QC | Basis set | Active space | States Ne/Ne$^+$ | X2C |
|---|---|---|---|---|
| I | [7$s$6$p$3$d$2$f$] | RAS(8; 1, 1) | 41/132 | No |
| II | [22$s$6$p$3$d$2$f$]-rcc | RAS(8; 1, 1) | 41/132 | Yes |
| III | [9$s$8$p$5$d$4$f$] | RAS(26; 1, 1) | 131/420 | No |

coupling against the popular choice to account only for the two-electron terms in Eq. (12), denoting them as $\mathcal{H}$ and $r^{-1}$ coupling, respectively. The combination of matrix elements corresponding to each approach is detailed in Appendix B.

To sum up, the present paper reports on the influence of different combinations of the introduced approximations to the potentials, transition matrix elements, and continuum orbitals on the partial Auger decay rates of the exemplary neon $1s^{-1}3p$ resonance. As a shorthand notation for the combination of the different approximations we will use the (coupling)-(potential)-(nonorthogonality) notation, where applicable. For instance, $\mathcal{H}$-$V_f^{\mathrm{JX}}(r)$-NO denotes partial rates obtained using the $\mathcal{H}$ coupling, with radial waves corresponding to the $V_f^{\mathrm{JX}}(r)$ potential and including the overlap terms.

## IV. COMPUTATIONAL DETAILS

### A. Quantum chemistry for bound states

The wave functions of the bound neutral and ionic states have been obtained in separate state-averaged RASSCF calculations with a locally modified version of MOLCAS 8.0 [78]. To prevent mixing of different angular momentum basis functions into one orbital, the "atom" keyword has been employed. The QC schemes used to evaluate the bound states $|\Psi_i\rangle$ and $|\Psi_f^+\rangle$ are presented in Table I. The RAS formalism is a flexible means to select electronic configurations. Therein, the AS is subdivided into three subspaces RAS1, RAS2, and RAS3. The RAS notation that is used throughout the paper is to be understood as follows. In all spaces, the $1s$ orbital forms the RAS1 subspace and the $2s$ and $2p$ orbitals build up the RAS2 one. The occupation of the $2s$ and $2p$ orbitals in RAS2 is not restricted, while only $h$ electrons may be removed from RAS1. Finally the RAS3 subspace contains $v$ virtual orbitals that can be occupied by at most $p$ electrons. Thus, we can herein uniquely specify each AS as RAS($v$; $h$, $p$). The ASs used in this paper are as follows: RAS(8; 1, 1), containing $3s$, $3p$, $4s$, and $4p$ orbitals in the RAS3; RAS(26; 1, 1), enlarging RAS3 by the $3d$, $4d$, $5s$, $5p$, $6s$, and $6p$ orbitals; and RAS(33; 1, 1), adding the $4f$ orbitals. The number of configurations possible with each AS is shown in Table II. For all QC schemes (see Table I) all states are included in the RASSCF procedure for

TABLE II. Maximum number of configurations for each AS.

| RAS | RAS(8; 1, 1) | RAS(26; 1, 1) | RAS(33; 1, 1) |
|---|---|---|---|
| Ne | 41 | 131 | 166 |
| Ne$^+$ | 197 | 629 | 797 |

the Ne wave functions, while the core excited states have been excluded for the calculations of Ne$^+$.

Atomic natural orbital (ANO) type basis sets have been employed using a (22$s$17$p$12$d$11$f$) primitive set. It was constructed by supplementing the ANO exponents for neon [79] in each angular momentum with eight Rydberg exponents generated according to the scheme proposed by Kaufmann *et al.* [80]. The contractions were then obtained with the GENANO module [81] of OPENMOLCAS [82] using density matrices from state averaged RASSCF calculations for Ne and Ne$^+$ with the RAS(33; 1, 1) AS. All 166 possible states for Ne have been taken into account, but for Ne$^+$ the core excited manifold has been excluded, leading to 532 states. To get the final basis set, the sets obtained for Ne and Ne$^+$ have been evenly averaged. In this paper, we use the following contractions: [7$s$6$p$3$d$2$f$], obtained by the procedure described above; [9$s$8$p$5$d$4$f$], corresponding to [7$s$6$p$3$d$2$f$] supplemented with Rydberg contractions that resulted from the GENANO procedure using the "rydberg" keyword; and [22$s$6$p$3$d$2$f$]-rcc, similiar to [7$s$6$p$3$d$2$f$] but with uncontracted $s$ functions and scalar relativistic corrections according to the exact two component decoupling (X2C) scheme [83] (see Supplemental Material [77]).

All energies have been corrected using the single state RASPT2 method [84] with an imaginary shift of 0.01 a.u. To be consistent with the basis set generation, scalar relativistic effects have only been included for QC II. The RAS state interaction [85] module of MOLCAS was used to compute the biorthonormally transformed orbital and CI coefficients [86] for the atomic and ionic states: $\{\varphi_i\}, \{C_j\} \rightarrow \{\tilde{\varphi}_i\}, \{\tilde{C}_j\}$ such that $\langle\tilde{\varphi}_i^+|\tilde{\varphi}_j\rangle = \delta_{ij}$, while the total wave functions remain unchanged. This biorthonormal basis is used in the evaluation of the Dyson orbitals [Eqs. (14), (B3), and (B4)] and two-electron reduced transition densities [Eq. (17)].

### B. Matrix elements in the atomic basis

The matrix elements between bound orbitals occurring in Eqs. (12), (15), and (16) are evaluated by transforming the orbitals to the atomic basis and calculating the atomic basis integrals with the LIBCINT library [87]. The most time consuming part in the computation of the partial decay rates using Eq. (12) is the estimation of the two-electron continuum-bound integrals. Transforming the two-electron reduced transition densities and the orbitals to the atomic basis $\{\chi_i\}$ and neglecting the spin integration, the two-electron continuum-bound integrals used in the practical evaluation of Eq. (16) read as

$$\langle\alpha a|bc\rangle = \int \psi_\alpha^*(\mathbf{r}_1)\chi_b(\mathbf{r}_1)\underbrace{\left[\int \frac{\chi_a^*(\mathbf{r}_2)\chi_c(\mathbf{r}_2)}{r_{12}})d\mathbf{r}_2^3\right]}_{f_{ac}(\mathbf{r}_1)}d\mathbf{r}_1^3.$$

(18)

The function $f_{ac}(\mathbf{r}_1)$ is similar to an atomic nuclear attraction integral and is evaluated as a function of $\mathbf{r}_1$ using the LIBCINT library [87]. An important point is to exploit the fact that the kinetic energy of the continuum electron is only encoded in its radial part. Transforming to spherical coordinates $\mathbf{r} \rightarrow (r, \Omega)$ centered at the origin of the outgoing electron allows one to

separate off the radial integration:

$$\langle \alpha a | bc \rangle = \int_0^\infty r w_l^{fk}(r)$$

$$\times \underbrace{\left[ \int_\Omega Y_l^m(\Omega) \chi_b(\mathbf{r}(r, \Omega)) f_{ac}(\mathbf{r}(r, \Omega)) d\Omega \right]}_{F_{abc}(r)} dr. \tag{19}$$

The angular integral in $F_{abc}(r)$ is determined numerically by using the adaptive two-dimensional integration routine CUHRE from the CUBA 4.2 library [88]. To reduce the number of points at which $F_{abc}(r)$ is evaluated, an adaptive spline interpolation is used, which was developed by us and implemented in our code. Therein, the grid spacing is adjusted such that the absolute error estimate of the interpolation is kept lower than $10^{-6}$ a.u. on each region with a different spacing. Note that the $F_{abc}(r)$ are determined only once, while the final radial integration in Eq. (19) needs to be evaluated for every transition $i \to \alpha$. The radial integration in Eq. (19) is carried out using the Simpson rule. For the one-electron continuum-bound integrals that are needed in the evaluation of the one-electron matrix elements in Eq. (12), an analogous approach has been implemented. This protocol has been developed aiming for the application to molecular systems. Hence, it does not exploit that the atomic orbitals are eigenstates of angular momentum operators, which would be usual in a purely atomic approach.

## V. RESULTS AND DISCUSSION

Here, we perform a thorough benchmark of the approaches to evaluate AES presented in Sec. II on the exemplary Auger decay of the neon $1s^{-1}3p$ resonance. First, in Sec. V A, we compare the AES modeled with our protocol against data obtained from an atomic MCDF calculation [68], which serves as a high level theoretical reference. Second, in Sec. V B, we undertake the comparison to experimental results. The comparison against both theory and experiment is needed since no uniform and highly resolved experimental data covering the full energy range discussed herein have been published to date.

### A. Benchmark of theoretical models

Panel (a) of Fig. 2 shows neon AESs, resulting from the autoionization of the $1s^{-1}3p$ states, obtained using bound-state wave functions from QC scheme I (see Table I) with radial waves corresponding to the spherically averaged direct-exchange potential $V_f^{JX}(r)$ [Eq. (7e)]. The partial rates have been evaluated using the full $\mathcal{H}$ coupling as well as the approximate $r^{-1}$ coupling in Eq. (12). Further, the nonorthogonality of the continuum and bound orbitals was accounted for by including the overlap terms, NO [see Eqs. (13), (15), and (16)]. A spectrum employing $r^{-1}$ coupling at the MCDF level, obtained by Stock *et al.* [68] with the RATIP package [22], serves as a theoretical benchmark. Therein, the atomic structure was obtained with a configuration space including single-electron excitations from the $1s$, $2s$, and $2p$ to the $np$ up to $n = 7$ and $3d$ orbitals. The four-component continuum

orbitals have been obtained as distorted waves within the potential of the respective ionized atomic state.

All spectra have been constructed by assigning a Gaussian line shape with a full width at half maximum (FWHM) of $\gamma = 0.1$ eV to each channel:

$$\text{AES}_{1s^{-1}3p}(\varepsilon) = \sum_\alpha \Gamma_{1s^{-1}3p\alpha} G(\varepsilon - \varepsilon_\alpha, \gamma), \tag{20}$$

where $G(\varepsilon, \gamma) = \sqrt{\ln 2/(\pi\gamma)} \exp(-4\ln 2\varepsilon^2/\gamma^2)$, $\varepsilon$ is the kinetic energy of the emitted electrons, and $\varepsilon_\alpha = \mathcal{E}_{1s^{-1}3p} - \mathcal{E}_f$ is the Auger electron energy of the channel $|\Psi_\alpha\rangle$. The spectra were normalized to the peak height at 811.5 eV, and shifted globally by $-5.35$ eV (QC I) and $-2.45$ eV (MCDF) such that the peak at 811.5 eV is aligned to the experimental data taken from Kivimäki *et al.* [69] (see Fig. 4). In addition, the dominant continuum orbital angular momentum contribution to the intensity is indicated for each peak. This shows that the regions 743–765, 765–800, and 800–825 eV correspond almost exclusively to the emission of $s$, $p$, and $d$ waves, respectively, with the exception that the peaks at 803 and 808 eV lie in the $d$ region but are due to $s$-wave emission. Hence, we will refer to these regions as $s$, $p$, and $d$, rather than using the energies, in what follows.

It is evident from Fig. 2(a) that the normalized AESs obtained for the $\mathcal{H}$ and $r^{-1}$ couplings are almost indistinguishable in the $s$ and $d$ regions. In contrast, the features in the $p$ region at 771 and 776 eV are enhanced by 10%, while the small bands in the range 783–788 eV are reduced by about 40%, if the $\mathcal{H}$ coupling terms are included. The overall effect on the spectrum, however, is still rather small and neglecting the contributions beyond the $r^{-1}$ coupling in the partial rate evaluation seems to be justified in this case. The comparison with the MCDF data in the $d$ region shows that the Auger energies and relative intensities are overall quite well reproduced by our approach. Only the intensities of two small satellite peaks at 803 and 809 eV are overestimated and three tiny features around 805.5–807.5 eV are not present when using our approach. The latter deficiency can be safely attributed to the smaller configuration space employed in the QC I scheme as compared to the one used to obtain the MCDF results in [68]. Looking at the $s$ and $p$ regions, the Auger energies from the QC model I become slightly but increasingly blueshifted with respect to the MCDF ones at the lower-energy flank of the spectrum. The intensities in turn are considerably overestimated by factors of about 5 and 2 for the $s$ and $p$ regions, respectively. Note that very similar spectra are obtained if the RASPT2 energy correction is not used (see Supplemental Material [77] Fig. S1).

Panels (b) and (c) of Fig. 2 show the integrated decay rates for the $s$, $p$, and $d$ regions evaluated using QC model I with the $r^{-1}$ (b) and $\mathcal{H}$ (c) couplings, comparing different approaches to compute the partial decay rates. The respective spectra are given in Supplemental Material [77] Figs. S2–S7. The rates were obtained for all combinations of potential models in Eqs. (7a)–(7e) with the different nonorthogonality approaches SO, NO, and GS for the continuum orbitals. Since no absolute rates for the MCDF results are available, these have been scaled to the total decay rate obtained using the $r^{-1}$-$V_f^{JX}(r)$-NO treatment. The data in panels (b) and (c) show
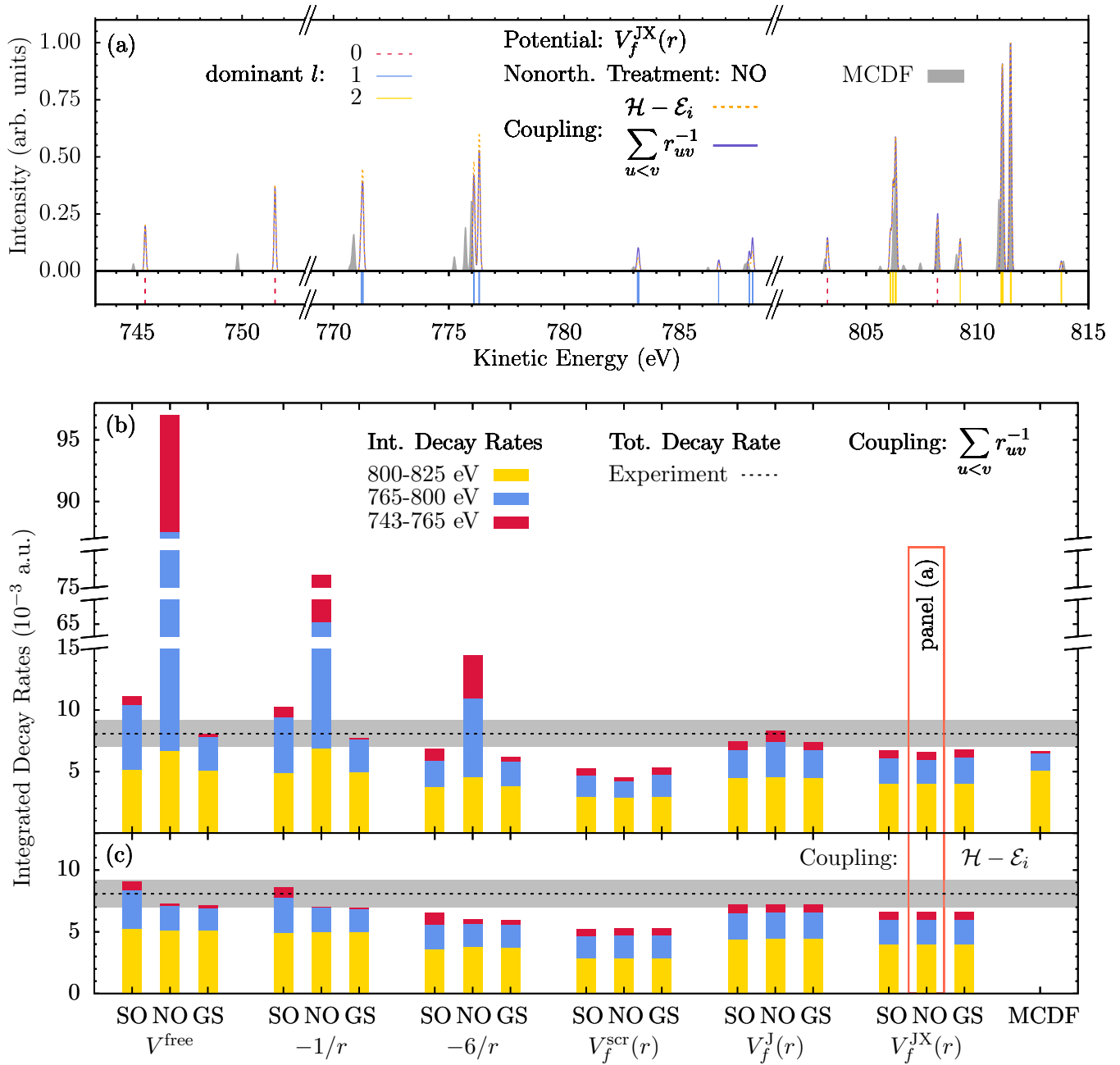
FIG. 2. (a) Neon $1s^{-1}3p$ AES obtained with the $r^{-1}$ and $\mathcal{H}$ couplings and the NO approach using continuum orbitals generated by the $V_f^{\mathrm{JX}}(r)$ potential are shown in comparison to the MCDF results reported by Stock *et al.* [68]. All spectra are broadened using a Gaussian profile with an FWHM of 0.1 eV, normalized to the peak at 811.5 eV, and shifted globally to align the 811.5-eV peak with experimental data [69]. The spectra from panel (a) correspond to the NO histograms of the $V_f^{\mathrm{JX}}(r)$ potential in panels (b) and (c). The vertical lines at the bottom of panel (a) indicate the predominant continuum orbital angular momentum ($l$) contribution to each peak. (b), (c) Auger decay rates integrated over the given energy ranges corresponding to distinct $l$ contributions. The decay rates have been evaluated based on QC model I for the $r^{-1}$ (b) and $\mathcal{H}$ (c) couplings. The radial continuum functions correspond to the depicted potentials. Nonorthogonality of the continuum and bound orbitals was treated with the SO, NO, and GS approaches (see text). The MCDF data have been scaled such that the total decay rate matches the one obtained for the $r^{-1}$-$V_f^{\mathrm{JX}}(r)$-NO approach. For reference, the experimentally determined total rate of $8.08 \pm 1.1 \times 10^{-3}$ a.u. $(0.22 \pm 0.03$ eV) [89] is depicted as a horizontal dashed line. The gray region indicates the experimental uncertainty.

that the decay rates corresponding to the $s$, $p$, and $d$ spectral regions converge for both couplings as the quality of the potential is increased from the free-particle approximation $V^{\mathrm{free}}$ to the spherically averaged direct-exchange potential $V_f^{\mathrm{JX}}(r)$. The $s:p:d$ ratio obtained from the MCDF spectrum,

however, is not matched. Our approaches systematically overestimate the decay rates due to the $s$ and $p$ channels, in line with the mismatch of intensities unveiled in panel (a).

Prominently, using the approximate $r^{-1}$ coupling together with the NO overlap terms leads to an overestimation of the

$s$ and $p$ regions with respect to the SO results by an order of magnitude for $V^{\text{free}}$ and $-1/r$, and by factors of 4 and 3 for $-6/r$. In contrast, employing the SO approximation or GS orthogonalized continuum orbitals results in more realistic decay rates. Here, the GS rates reproduce the SO ones for the $d$ region but are considerably smaller in the $s$ and $p$ regions. However, when either of the more physically sound potentials $V_f^{\text{scr}}(r)$, $V_f^{\text{J}}(r)$, or $V_f^{\text{JX}}(r)$ is used, the choice of the nonorthogonality treatment has only a weak influence on the integrated decay rates. This characteristic is due to the continuum-bound orbital overlaps that decrease if more realistic potentials are chosen, causing the NO overlap terms in Eqs. (13), (15), and (16) as well as the effect of the GS orthogonalization to become negligible. Adding to this, the general insensitivity of the $d$ region to the nonorthogonality treatment is explained by the fact that the overlap of the $d$ continuum waves with the bound orbitals vanishes independently of the potential model. The overlap integrals are given in Supplemental Material [77] Table S1.

Generally, the inclusion of the $\mathcal{H}$ coupling, Fig. 2(c), yields mostly smaller total decay rates and less pronounced differences between the SO, NO, and GS results. The SO decay rates are usually the largest when $\mathcal{H}$ coupling is applied, while the NO and GS ones are smaller, underestimating the $s$ and $p$ regions for $V^{\text{free}}$, $-1/r$, and $-6/r$, with respect to SO. Noteworthy, the huge overestimation due to the combination of $r^{-1}$ coupling and NO terms is mitigated completely. The reason is that the NO contribution to the matrix element is determined by cancellation effects between different one- and two-electron NO terms rather than their individual magnitude. Neglecting the one-electron contributions in $r^{-1}$ coupling prohibits this error cancellation, leading to the immense overestimation observed for $V^{\text{free}}$, $-1/r$, and $-6/r$. Similarly, the agreement between the GS and NO results for these potentials is not because the effect of the GS orthogonalization is minute, but again due to the cancellation.

We conclude the discussion of this figure with the observation that the total rates obtained with the $V_f^{\text{J}}(r)$ and $V_f^{\text{JX}}(r)$ potentials reproduce the experimentally observed decay rate [89]. Independent of the chosen approach, the best match is obtained with the $V_f^{\text{J}}(r)$ potential, whereas the $V_f^{\text{JX}}(r)$ potential leads to slightly underestimated total rates, which can be attributed to the inclusion of the attractive exchange term, Eq. (A5). Similarly, we assign the considerable underestimation of the total decay rates by the $V_f^{\text{scr}}(r)$ potential to the fact that it is more attractive in the core region than $V_f^{\text{JX}}(r)$ (see Fig. 3). The $-6/r$ potential yields total rates and spectra that are in approximate agreement with those obtained for $V_f^{\text{J}}(r)$ and $V_f^{\text{JX}}(r)$ apart from the case when $r^{-1}$ coupling and the NO terms are used (spectra in Supplemental Material [77] Figs. S2–S7). Notably, the total rates obtained in $\mathcal{H}$ coupling with the effective potentials $V^{\text{free}}$ and $-1/r$ agree well with the experimental reference. However, despite the good agreement in the total rates the spectra for these approaches deviate in the $p$ region considerably from the ones obtained for the more accurate potentials (see Supplemental Material [77] Figs. S5–S7), indicating that this agreement is rather accidental.

To shed light on the influence of different potentials on the total decay rates and spectra obtained with QC model

I, $\mathcal{H}$ coupling, and the NO approach, potentials, radial continuum functions, and spectra are presented in Fig. 3. Panel (a) contains the normalized AESs obtained using the potentials $-1/r$, $-6/r$, $V_f^{\text{scr}}(r)$, and $V_f^{\text{JX}}(r)$. The spectra have been shifted vertically for the sake of clarity. Shifts and broadening parameters are the same as in Fig. 2(a). The $d$ region is represented very well with all potential models, with the exclusion that the satellite bands at 803 and 808 eV are barely present when using the $-1/r$ potential. In contrast, the relative intensities of the $s$ and $p$ regions of the spectra are strongly affected by the choice of the potential. Here, the $p$ region consists of two peak groups with different character. Using the $V_f^{\text{JX}}(r)$ results as a reference for this discussion, the peaks around 771 and 776 eV are overestimated by 30% with $V_f^{\text{scr}}(r)$, almost reproduced with $-6/r$ and underestimated by a factor of 4 when using $-1/r$. In contrast, the bands between 783 and 788 eV behave in an inverse manner. Namely, they are underestimated by 50% with $V_f^{\text{scr}}(r)$ and overestimated by 50% and a factor of 4 with $-6/r$ and $-1/r$, respectively. This behavior of the screened and the effective Coulomb potentials is caused by the fact that $V_f^{\text{scr}}(r)$ is more attractive and $-1/r$ as well as $-6/r$ are less attractive than $V_f^{\text{JX}}(r)$, as depicted in panels (b)–(d). This trend is solely dictated by the potential but not the coupling or nonorthogonality treatment; note the exception of the $r^{-1}$-NO combination (see Supplemental Material [77] Figs. S2–S7). Finally, in the $s$ region, the tighter potential results in larger intensities: $-1/r$ and $-6/r$ lead to an underestimation by an order of magnitude and 35%, respectively, whereas $V_f^{\text{scr}}(r)$ yields an overestimation by 25%.

For each region, the radial waves and respective potentials, including the angular momentum term, are shown in panels (b)–(d) corresponding to the characteristic peaks denoted in panel (a). Note that the $V^{\text{free}}$ and $V_f^{\text{J}}(r)$ cases are very similar to the $-1/r$ and $V_f^{\text{JX}}(r)$ ones, respectively, and have been excluded from the discussion of this figure. The respective spectra are given in Supplemental Material [77] Fig. S7. One might understand the differences in the sensitivity of the $s$, $p$, and $d$ spectral regions to the potential by comparing the short-range behavior of the radial waves $w_l^{fk}(r)/r$ [Eq. (11a)] with the electron density that is sharply peaked in the core region. This suggests that the matrix elements in Eq. (12) are very sensitive to the description of the continuum orbitals in this region. It is well known that only the $s$ waves have a considerable contribution at the core, since the radial functions tend to zero as $r^l$. In fact, the effective radial potential at the core is dominated by the angular momentum term for $l > 0$, meaning that the influence of the present potential models on the total rates should decrease with increasing $l$. Regarding the relative changes of the integrated decay rates within each region, this is true for $\mathcal{H}$ and $r^{-1}$ coupling, when the NO overlap terms are included, irrespective of whether the GS orthogonalization is used in addition or not [Figs. 2(b) and 2(c)]. However, under the SO approximation for $r^{-1}$ coupling, the $p$ spectral region is more sensitive to variations in the potential model than the $s$ region. In fact, for the $s$ waves it is seen that only the potentials $V_f^{\text{scr}}(r)$ and $V_f^{\text{JX}}(r)$ lead to similar radial waves, the slight differences being due to the fact that the screening model is too attractive in the core region.
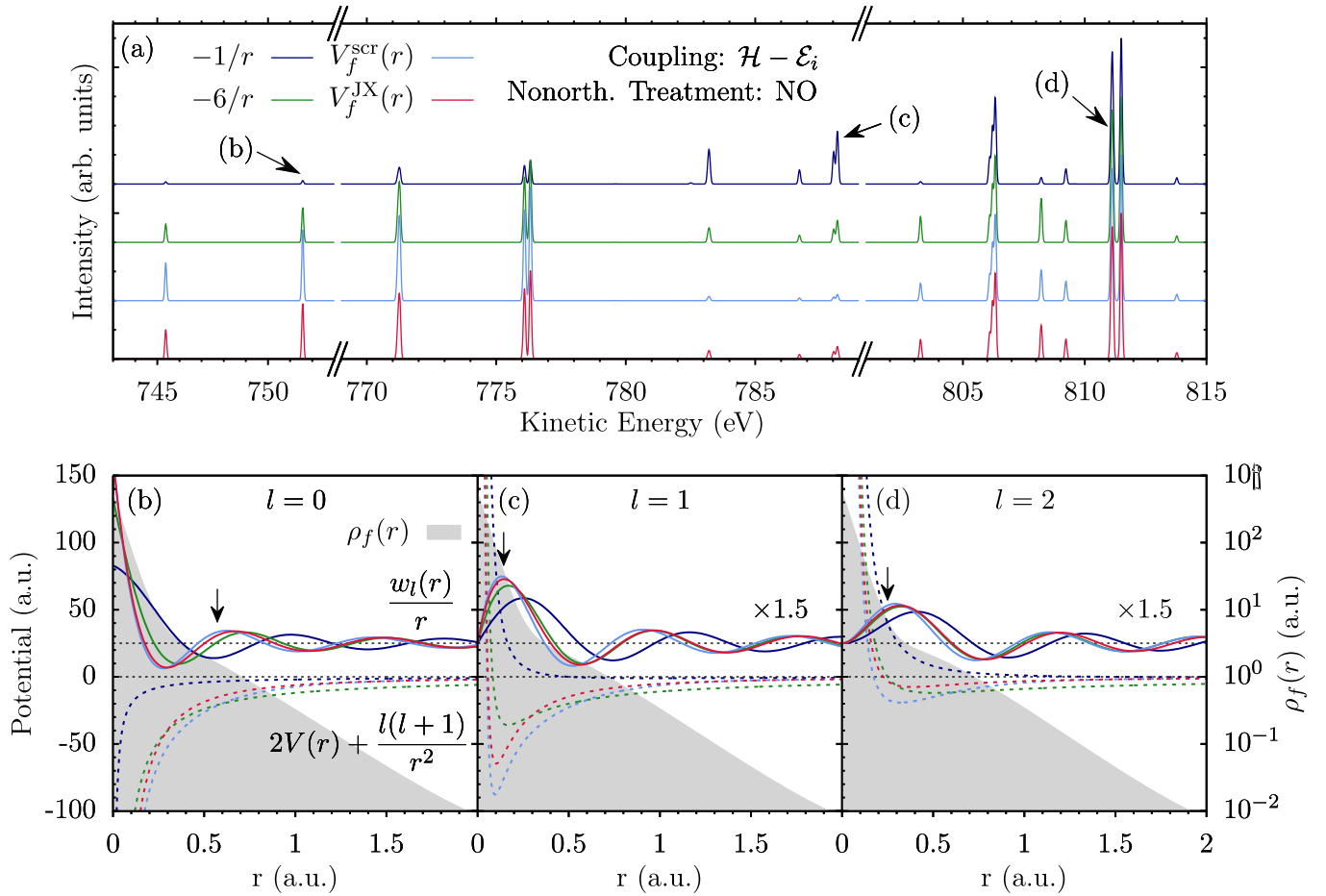
FIG. 3. (a) Neon $1s^{-1}3p$ AES evaluated using QC scheme I, $\mathcal{H}$ coupling, and the NO nonorthogonality treatment with radial continuum functions corresponding to the given potentials. The spectra are normalized to the peak at 811.5 eV, broadened using a Gaussian FWHM of 0.1 eV, and shifted globally by $-5.35$ eV. In addition, they have have been shifted vertically by 2.0 [$V_f^{\mathrm{scr}}(r)$], 4.0 ($-6/r$), and 6.0 ($-1/r$) units to enhance the visibility. (b–d) Effective radial potentials (dashed) and continuum functions (solid) corresponding to the dominant angular momentum contribution $l = 0$, 1, 2 of the peaks (b)–(d) in panel (a) are shown together with the spherically averaged electron densities $\rho_f(r)$ of the respective ionized states. The colors of the radial waves and potentials correspond to the spectra shown in panel (a). At the positions indicated by the arrows in panels (b)–(d), the radial waves correspond to (top to bottom) $V_f^{\mathrm{scr}}(r)$, $V_f^{\mathrm{JX}}(r)$, $-6/r$, and $-1/r$. In the region of potential minima, the effective potentials are ordered (from top to bottom) as $-1/r$, $-6/r$, $V_f^{\mathrm{JX}}(r)$, and $V_f^{\mathrm{scr}}(r)$.

Notably, these slight deviations lead to an underestimation of the total decay rates obtained with the $V_f^{\mathrm{scr}}(r)$ potential by about 25% in comparison to those obtained for $V_f^{\mathrm{JX}}(r)$ (see Fig. 2), underlining the sensitivity of the total decay rates to the choice of the model potential.

The effective Coulomb potential $-1/r$ provides a qualitatively incorrect description in both the core and outer regions, whereas the $-6/r$ potential leads to a sort of compromise in accuracy. It describes the core region much better than the $-1/r$ potential but as a tradeoff has an incorrect asymptotic behavior in the valence region. For all but the $r^{-1}$-NO approaches this suffices to predict spectra that are in qualitative agreement with the ones obtained for $V_f^{\mathrm{JX}}(r)$, whereas using the $-1/r$ potential is only justified for the main features of the $d$ region (see Supplemental Material [77] Figs. S2–S7). If one is interested in the full spectrum, one should use a model taking into account the electronic potential of the ionized core, such as $V^{\mathrm{scr}}(r)$, $V_f^{\mathrm{J}}(r)$, or $V_f^{\mathrm{JX}}(r)$.

Summarizing the discussion up to this point, it seems that satisfactory total decay rates and AESs are only obtained with the potentials $V_f^{\mathrm{J}}(r)$ and $V_f^{\mathrm{JX}}(r)$. Further, employing $r^{-1}$ coupling and the SO approximation seems to be very well justified for these models and we will use these in the comparison against experimental data below. Generally, special caution has to be taken with the inclusion of the NO overlap terms for simple potential models. While the results obtained using $\mathcal{H}$ coupling greatly profit from error cancellation, this is not the case for $r^{-1}$ coupling, where the NO terms strongly emphasize the deficiencies of an approximate potential. In addition, it remains to be clarified whether these cancellation effects are a general feature or a peculiarity of the neon $1s^{-1}3p$ AES.

### B. Comparison to experimental data

In this section, the comparison of our theoretical results to the experimental data in the full spectral range is presented. In addition, to unravel the influence of the underlying QC onto
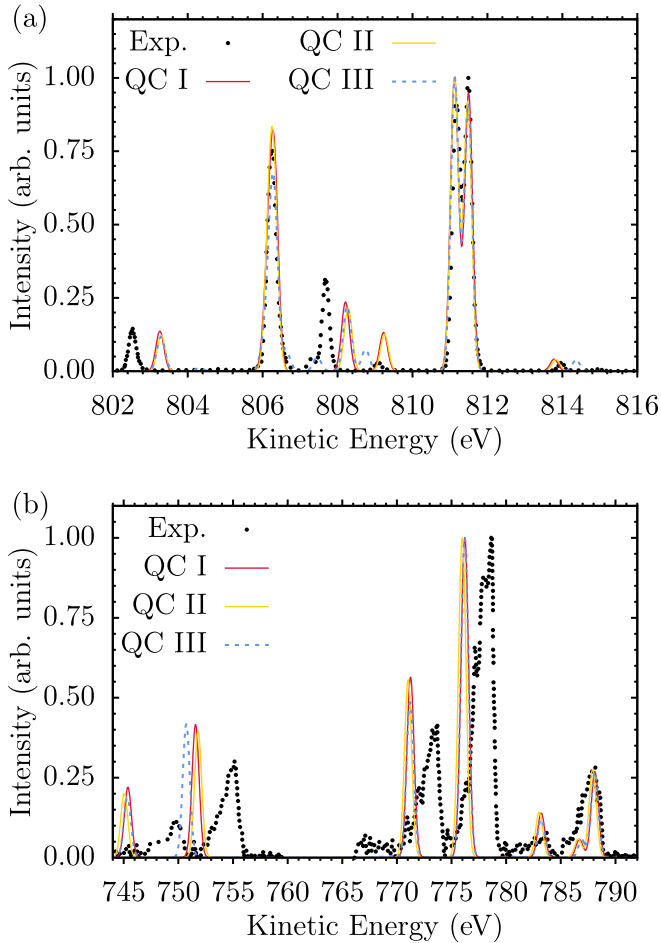
FIG. 4. Comparison of experimental and theoretical neon $1s^{-1}3p$ AES obtained based on the QC schemes I–III with the $r^{-1}$-$V_f^{JX}(r)$-SO method. The spectra obtained with QC I, II, and III have been shifted by $-5.35$, $-4.75$, and $-5.18$ eV, respectively, to align the peak at 811.5 eV with the experimental data in panel (a). To account for the different line shapes of the experimental spectra that have been digitalized from [69] (a) and [70] (b), broadening with a Gaussian FWHM of 0.25 and 0.77 eV was used in panels (a) and (b), respectively. Further, the spectra have been normalized individually to the peaks at 811.5 eV (a) and 776 eV (b).

the AES, we discuss spectra obtained with the QC schemes I–III as described in Table I. The QC model II, which is more sophisticated than QC I, contains an uncontracted $s$ basis and accounts for scalar relativistic effects, whereas QC III employs an active space larger than in QC I.

To the best of our knowledge, no experimental Auger emission spectrum of the neon $1s^{-1}3p$ resonance that covers the full spectral range presented in Figs. 2 and 3 has been published to date. Hence, in Fig. 4 the spectra obtained with the QC models I–III and the $r^{-1}$-$V_f^{JX}(r)$-SO approach are compared against experimental data taken from Kivimäki *et al.* [69], for the $d$ region (a), and Yoshida *et al.* [70], for the $s$ and $p$ regions (b). Note that the $\mathcal{H}$-$V_f^{JX}$-NO approach does not lead to a considerable improvement of the agreement with the experimental data, as shown in Supplemental Material [77] Fig. S9. The spectra have been shifted by $-5.35$, $-4.75$, and

$-5.18$ eV for QC models I, II, and III to align the peaks at 811.5 eV. In panel (a), the spectra have been broadened using a Gaussian profile with an FWHM of 0.25 eV, corresponding to the line shape of the peak at 806.5 eV in the experimental spectrum. Further, in panel (b) a Gaussian FWHM of 0.77 eV was chosen to represent the shape of the high-energy flank of the asymmetric peak at 778.5 eV in the experimental spectrum. Additionally, the spectra have been normalized to the heights of the main peaks at 811.5 eV (a) and 776 eV (b). Finally, the experimental data have been recorded at angles of 54.7° (a) and 56° (b) to the polarization vector. Data for these angles have been chosen to rule out anisotropy effects, which makes the comparison with our angle integrated spectra easier.

Panel (a) shows that the agreement between the experimental and the theoretical spectra is fairly good. In fact, the relative energetic positions and intensities of the main peaks are reproduced quite well. However, smaller satellite peaks at 803 and 808.2 eV are blueshifted by about 0.5 eV. Generally, the agreement between theory and experiment is worse for the smaller features, although an unambiguous assignment is still possible. Using the uncontracted $s$ basis and including scalar relativistic effects in QC II does not influence the resulting spectrum. In turn, the larger active space incorporated in the QC scheme III leads to a better reproduction of some tiny features at 806.4, 807.5, and 808.8 eV. The blueshifts of the peaks already present with QC I and II are not affected, when employing QC III.

The comparison of the spectra covering the $s$ and $p$ regions with the experimental data is shown in panel (b). Here, the overall agreement is worse than in panel (a) concerning both the relative intensities and energetic positions of the peaks. Regarding the offset in energies, the low-energy part corresponds to transitions to the highest excited states of the ionic manifold, the energies of which are progressively overestimated. This is a typical situation when a smaller part of the electron correlation is recovered for the higher-lying states. Specifically, the positions of the peaks around 783 and 788 eV are reproduced well by all methods, while the intensity of the former, small peak is overestimated. Further, the peaks at 771 and 776 eV are redshifted by about 2 eV, and the relative intensity of the former is overestimated by approximately 30% (QC I and II) and 15% (QC III). Finally, the peaks at 745 eV and around 751 eV, corresponding to the $s$ region, are redshifted by 5 eV (QC I–III) and 4 eV (QC I and II) or 5 eV (QC III), respectively. The intensities of these peaks are overestimated by about 30% with respect to the experimental data. Hence, in the $s$ and $p$ regions, our results agree better with the experimental reference than with the MCDF spectrum. The total decay rates, however, are not visibly altered by the choice of either of the QC schemes I, II, or III (see Supplemental Material [77] Fig. S8).

To wrap up this discussion, we conclude that the RASSCF and RASPT2 electronic structure method combined with the $r^{-1}$-$V_f^{JX}$-SO approach to construct continuum orbitals and evaluate the transition matrix elements provides Auger energies and intensities for the decay of the neon $1s^{-1}3p$ resonance of a similar quality as those obtained in [68] with the MCDF approach. In particular, a straightforward assignment of experimental results is possible. Further, the inclusion of scalar relativistic effects into the one-component electronic

structure of the bound states has no notable influence on the spectra, while a large active space is necessary only to reproduce minor satellite features.

## VI. CONCLUSIONS AND OUTLOOK

In this paper, we have demonstrated an approach to the evaluation of autoionization rates on the example of the Auger decay from the neon $1s^{-1}3p$ resonance. The suggested protocol is based on the RASSCF and RASPT2 methods to evaluate the bound-state wave functions and energies, supplemented by a single-channel scattering model for the outgoing electron. Here, the single-center approximation is introduced to reduce the continuum orbital problem to the radial dimension by averaging over the angular structure of the ionized electron density. To model the true radial potential, six different models, $V^{\text{free}}$, $-1/r$, $-6/r$, $V_f^{\text{scr}}(r)$, $V_f^{\text{J}}(r)$, and $V_f^{\text{JX}}(r)$, have been discussed. Further, three different ways to account for the nonorthogonality of the continuum and bound orbitals, SO, NO, and GS, as well as the effect of using complete, $\mathcal{H}$, or approximate, $r^{-1}$, coupling in the partial rate evaluation have been investigated. All combinations of these sum up to 36 different variants to evaluate partial autoionization rates for an underlying bound-state QC calculation and have been implemented in a stand-alone program.

Here we compared all these approaches with respect to their ability to reproduce the experimental [69,70] as well as theoretical AES obtained at the fully relativistic MCDF level [68]. The applied quantum chemistry protocol allows for a fairly good reproduction of the transition energies if compared to the theoretical reference and experiments. However, intensities are more difficult to reproduce. Here, the quality of the continuum orbital was shown to be the most important issue as it strongly influences the obtained AESs. Especially the core part of the ionic potential is of importance for AES. The effect of the potential is closely connected to the angular momentum of the outgoing electron as it governs the extent of the continuum orbital into the core region. For instance, we found that the $d$ region of the spectrum is rather insensitive to the choice of the model potential, whereas the $s$ and $p$ regions require one to use one of the potentials $V_f^{\text{scr}}(r)$, $V_f^{\text{J}}(r)$, and $V_f^{\text{JX}}(r)$. Still, the MCDF intensities can only be reproduced in the $d$ region of the spectrum, while they are overestimated in the $s$ and $p$ parts. Further, the free-particle model and the asymptotic Coulomb potential $-1/r$ fail to reproduce the complete spectrum. Interestingly, inclusion of the NO terms in addition to using $r^{-1}$ coupling in the SO approximation does not in general lead to improved spectra, but rather strongly emphasizes the deficiencies of the $V^{\text{free}}$, $-1/r$, and $-6/r$ potentials. Due to pronounced error cancellation, however, this is diminished to a large extent if the $\mathcal{H}$ coupling is used with the NO terms. Remarkably, the effective $-6/r$ potential yields qualitative agreement with the spectra obtained using the more accurate potentials for all approaches but the aforementioned combination of $r^{-1}$ coupling and NO terms. In contrast, the spectra obtained with $V_f^{\text{scr}}(r)$, $V_f^{\text{J}}(r)$, and $V_f^{\text{JX}}(r)$ are weakly affected by the choice of both the coupling and nonorthogonality treatment. Since it remains unclear whether the cancellation effects observed

when using $\mathcal{H}$ coupling with the NO terms are a general feature, or a peculiarity of the neon AES, the NO terms should only be employed with caution. Generally, they should only be used if the descriptions of the potential and radial waves are sufficiently accurate. When dealing with approximate potentials, however, our results suggest to employ the SO or GS approaches, that seem to be less sensitive to the quality of the continuum orbital. In addition, due to the computational simplicity, the SO approximation could be preferred.

The comparison with experimentally obtained spectra using the $r^{-1}$-$V_f^{\text{JX}}(r)$-SO approach demonstrated the ability of the present method to accurately predict the neon $1s^{-1}3p$ AES, allowing a straightforward assignment of the experimental data. Interestingly, the general structure of the spectrum can be already reproduced quite well using a rather small active space, and is not sensitive to the inclusion of scalar relativistic effects. The best agreement with the experimental data is achieved by using a larger active space, including additional excitations to $3d$, $5s$, $5p$, $6s$, and $6p$ orbitals together with the spherically averaged direct exchange potential $V_f^{\text{JX}}(r)$. In addition our approach not only reproduces the experimentally measured AESs but the total decay rates of the neon $1s^{-1}3p$ resonance as well, when the potentials $-6/r$, $V_f^{\text{J}}(r)$, and $V_f^{\text{JX}}(r)$ are used. Since using the screened charge potential $V_f^{\text{scr}}(r)$ leads to notably underestimated absolute rates and is not computationally cheaper than using either $V_f^{\text{J}}(r)$ or $V_f^{\text{JX}}(r)$, providing a better accuracy, the latter two should be preferred.

Molecular systems can be treated with the presented method as well; however, in this case the molecular continuum has to be approximated by a single-centered spherically symmetric model. To keep the errors due to this approximation as small as possible, our findings suggest to use the $r^{-1}$ coupling together with the SO approximation to evaluate molecular AIS. The potentials should be modeled using either the direct $V_f^{\text{J}}(r)$ or direct-exchange $V_f^{\text{JX}}(r)$ variant. The applicability of these approximations has to be tested for the molecular case.

Currently our code is interfaced to the MOLCAS/OPENMOLCAS as well as to the GAUSSIAN program packages, allowing one to evaluate PES and AIS based on bound-state calculations conducted with the RASSCF and RASPT2 [65] as well as the linear-response time-dependent density functional theory method [90]. A paper discussing the applicability of the present models to treat molecular systems will follow.

## APPENDIX A: OBTAINING THE MODEL POTENTIALS

For the state-dependent models, Eqs. (7c)–(7e), the central quantity is the spherically averaged electron density of the

ionized state:

$$\rho_f(r) = \frac{1}{4\pi} \int_0^{4\pi} \rho_f(\mathbf{r}) \, d\Omega. \tag{A1}$$

It determines the potentials in the following way. The screened charge $Z_f(r)$ in Eq. (7c) is evaluated as the difference between the nuclear charge $Z$ and the integrated number of electrons present in a sphere with radius $r$ around the atom:

$$Z_f(r) = Z - \int_0^r \rho_f(r') r'^2 dr'. \tag{A2}$$

Further, the direct Coulomb potential of the ionized states in Eqs. (7d) and (7e) is the electrostatic potential of the

spherically averaged electron density $\rho_f(r)$:

$$J_f(r) = J_f(0) - \frac{4\pi}{r} \int_0^r dr' \int_0^{r'} r'' \rho_f(r'') dr''. \tag{A3}$$

$J_f(0)$ is defined by the asymptotic value of the integral over $r''$ in Eq. (A3):

$$\frac{J_f(0)}{4\pi} = \lim_{r' \to \infty} \int_0^{r'} r'' \rho_f(r'') dr''. \tag{A4}$$

Finally, a radial Slater-type exchange [73],

$$X_f^S(r) = -3\left(\frac{3}{8\pi}\rho_f(r)\right)^{\frac{1}{3}}, \tag{A5}$$

is employed.

### APPENDIX B: COUPLING MATRIX ELEMENTS

The total Auger transition matrix element $A_{i\alpha}^{\sigma M^+} = \langle \Upsilon_\alpha^{\sigma M^+} | \mathcal{H} - \mathcal{E}_i | \Psi_i \rangle$ reads

$$A_{i\alpha}^{\sigma M^+} = \underbrace{\langle \psi_{\alpha,\sigma} | h | \Phi_{i\alpha}^{M^+} \rangle + \sum_{q=1}^{N_{\mathrm{orb}}} \langle \psi_{\alpha,\sigma} \varphi_q^+ | \frac{1}{r_{12}} | \Xi_{i\alpha}^{M^+,q} \rangle}_{\mathrm{SO}} + \underbrace{\langle \psi_{\alpha,\sigma} | \tilde{\Phi}_{i\alpha}^{1,M^+} \rangle + \overbrace{\langle \psi_{\alpha,\sigma} | \tilde{\Phi}_{i\alpha}^{2,M^+} \rangle}^{r^{-1} \text{ coupling}} - \mathcal{E}_i \langle \psi_{\alpha,\sigma} | \Phi_{i\alpha}^{M^+} \rangle}_{\mathrm{NO}}. \tag{B1}$$

Here the contributions corresponding to the SO approximation, the NO terms, and the $r^{-1}$ coupling have been indicated. If the GS approach is used, $|\psi_{\alpha,\sigma}\rangle$ is replaced by

$$\left|\psi_{\alpha,\sigma}^{\mathrm{GS}}\right\rangle = \left|\psi_{\alpha,\sigma}\right\rangle - \sum_{i=1}^{N_{\mathrm{orb}}} \left\langle \varphi_{i,\sigma_i}^+ | \psi_{\alpha,\sigma} \right\rangle \left|\varphi_{i,\sigma_i}^+\right\rangle. \tag{B2}$$

The conjugated one- and two-electron Dyson orbitals are defined as

$$\left|\tilde{\Phi}_{i\alpha}^{1,M^+}\right\rangle = \sum_{q,s,t}^{N_{\mathrm{orb}}} \langle \varphi_q^+ | h | \varphi_s \rangle \langle \Psi_{f,M^+}^+ | (a_q^+)^\dagger a_s a_t | \Psi_i \rangle | \varphi_t \rangle \tag{B3}$$

and

$$\left|\tilde{\Phi}_{i\alpha}^{2,M^+}\right\rangle = \sum_{q_1 < q_2}^{N_{\mathrm{orb}}} \sum_{s_1 < s_2, t}^{N_{\mathrm{orb}}} \left( \langle \varphi_{q_1}^+ \varphi_{q_2}^+ | \frac{1}{r_{12}} | \varphi_{s_1} \varphi_{s_2} \rangle - \langle \varphi_{q_1}^+ \varphi_{q_2}^+ | \frac{1}{r_{12}} | \varphi_{s_2} \varphi_{s_1} \rangle \right) \langle \Psi_{f,M^+}^+ | (a_{q_1}^+)^\dagger (a_{q_2}^+)^\dagger a_{s_2} a_{s_1} a_t | \Psi_i \rangle | \varphi_t \rangle. \tag{B4}$$

Note that the sum of both terms, which occurs when the $\mathcal{H}$ coupling is used, takes the simple form

$$\left|\tilde{\Phi}_{i\alpha}^{1,M^+}\right\rangle + \left|\tilde{\Phi}_{i\alpha}^{2,M^+}\right\rangle = \mathcal{E}_f \left|\Phi_{i\alpha}^{M^+}\right\rangle, \tag{B5}$$

as demonstrated in [76], if the Hamiltonian eigenvalue equation $\mathcal{H}|\Psi_{f,M^+}^+\rangle = \mathcal{E}_f|\Psi_{f,M^+}^+\rangle$ is used. However, as detailed in the Supplemental Material [77] Sec. II, both approaches are strictly equivalent only if the occupied spin orbitals of the bound ionized and un-ionized wave functions span the same space. This is generally also not fulfilled for RASSCF orbitals if separate SCF procedures are used to obtain ionized and un-ionized states since the respective transformation properties between orbitals from different subspaces are lost. Moreover, the formulation of [76] cannot be applied to the $r^{-1}$ coupling case whereas our formulation can.

[1] V. G. Wentzel, Z. Phys. **43**, 524 (1927).

[2] P. Van der Heide, *X-Ray Photoelectron Spectroscopy: An In-troduction to Principles and Practices* (Wiley, New York, 2012).

[3] S. Hofmann, *Auger- and X-Ray Photoelectron Spectroscopy in Materials Science: A User-Oriented Guide*, Springer Series in Surface Sciences Vol. 49 (Springer, New York, 2013).

[4] S. Hüfner, *Photoelectron Spectroscopy: Principles and Applications* (Springer-Verlag, Berlin, 2003).

[5] L. Meitner, Z. Phys. **11**, 35 (1922).

[6] L. S. Cederbaum, J. Zobeley, and F. Tarantelli, Phys. Rev. Lett. **79**, 4778 (1997).

[7] J. Zobeley, R. Santra, and L. S. Cederbaum, J. Chem. Phys. **115**, 5076 (2001).

[8] P. Slavíček, N. V. Kryzhevoi, E. F. Aziz, and B. Winter, J. Phys. Chem. Lett. **7**, 234 (2016).

[9] P. Slavíček, B. Winter, L. S. Cederbaum, and N. V. Kryzhevoi, J. Am. Chem. Soc. **136**, 18170 (2014).

[10] M. A. Brown, M. Faubel, and B. Winter, Annu. Rep. Sect. C Phys. Chem. **105**, 174 (2009).

[11] V. Stumpf, K. Gokhberg, and L. S. Cederbaum, Nat. Chem. **8**, 237 (2016).

[12] H. Wang, T. Möhle, O. Kühn, and S. I. Bokarev, Phys. Rev. A **98**, 013408 (2018).

[13] F. de Groot and A. Kotani, *Core Level Spectroscopy of Solids* (CRC, Boca Raton, FL, 2008).

[14] R. W. Howell, Int. J. Radiat. Biol. **84**, 959 (2008).

[15] E. Alizadeh, T. M. Orlando, and L. Sanche, Annu. Rev. Phys. Chem. **66**, 379 (2015).

[16] R. F. Martin and L. E. Feinendegen, Int. J. Radiat. Biol. **92**, 617 (2016).

[17] A. Yokoya and T. Ito, Int. J. Radiat. Biol. **93**, 743 (2017).

[18] R. Neutze, R. Wouts, D. van der Spoel, E. Weckert, and J. Hajdu, Nature (London) **406**, 752 (2000).

[19] T. Åberg and G. Howat, in *Corpsucles and Radiation in Matter I*, edited by W. Mehlhorn, Encyclopedia of Physics Vol. 31 (Springer-Verlag, Berlin, 1982), p. 469.

[20] T. Åberg, Phys. Scr. **21**, 495 (1980).

[21] U. Fano, Phys. Rev. **124**, 1866 (1961).

[22] S. Fritzsche, Comput. Phys. Commun. **183**, 1525 (2012).

[23] H. Ågren, S. Svensson, and U. Wahlgren, Chem. Phys. Lett. **35**, 336 (1975).

[24] H. Ågren, J. Chem. Phys. **75**, 1267 (1981).

[25] I. Hillier and J. Kendrick, Mol. Phys. **31**, 849 (1976).

[26] M. Mitani, O. Takahashi, K. Saito, and S. Iwata, J. Electron Spectrosc. Relat. Phenom. **128**, 103 (2003).

[27] V. Carravetta, H. Ågren, O. Vahtras, and H. J. A. Jensen, J. Chem. Phys. **113**, 7790 (2000).

[28] B. Schimmelpfennig, B. Nestmann, and S. D. Peyerimhoff, J. Phys. B **25**, 1217 (1992).

[29] B. Schimmelpfennig, B. Nestmann, and S. Peyerimhoff, J. Electron Spectrosc. Relat. Phenom. **74**, 173 (1995).

[30] J. Oddershede, in *Advances in Chemical Physics*, edited by K. P. Lawley (Wiley, New York, 1987), pp. 201–239.

[31] C.-M. Liegener, Chem. Phys. Lett. **90**, 188 (1982).

[32] V. Averbukh and L. S. Cederbaum, J. Chem. Phys. **123**, 204107 (2005).

[33] P. Kolorenč, V. Averbukh, K. Gokhberg, and L. S. Cederbaum, J. Chem. Phys. **129**, 244102 (2008).

[34] P. Kolorenč and V. Averbukh, J. Chem. Phys. **135**, 134314 (2011).

[35] H. Siegbahn, L. Asplund, and P. Kelfve, Chem. Phys. Lett. **35**, 330 (1975).

[36] D. R. Jennison, Chem. Phys. Lett. **69**, 435 (1980).

[37] F. P. Larkins, L. C. Tulea, and E. Z. Chelkowska, Aust. J. Phys. **43**, 625 (1990).

[38] R. Fink, J. Electron Spectrosc. Relat. Phenom. **76**, 295 (1995).

[39] O. Travnikova, R. F. Fink, A. Kivimäki, D. Céolin, Z. Bao, and M. N. Piancastelli, Chem. Phys. Lett. **474**, 67 (2009).

[40] L. Inhester, K. Hanasaki, Y. Hao, S.-K. Son, and R. Santra, Phys. Rev. A **94**, 023422 (2016).

[41] Y. Hao, L. Inhester, K. Hansaki, and R. Santra, Struct. Dyn. **2**, 041707 (2015).

[42] K. Faegri and H. P. Kelly, Phys. Rev. A **19**, 1649 (1979).

[43] M. Higashi, E. Hiroike, and T. Nakajima, Chem. Phys. **68**, 377 (1982).

[44] K. Zähringer, H.-D. Meyer, and L. S. Cederbaum, Phys. Rev. A **45**, 318 (1992).

[45] P. V. Demekhin, D. V. Omel'yanenko, B. M. Lagutin, V. L. Sukhorukov, L. Werner, A. Ehresmann, K.-H. Schartner, and H. Schmoranzer, Opt. Spectrosc. **102**, 318 (2007).

[46] P. V. Demekhin, I. D. Petrov, V. L. Sukhorukov, W. Kielich, P. Reiss, R. Hentges, I. Haar, H. Schmoranzer, and A. Ehresmann, Phys. Rev. A **80**, 063425 (2009).

[47] P. V. Demekhin, A. Ehresmann, and V. L. Sukhorukov, J. Chem. Phys. **134**, 024113 (2011).

[48] L. Inhester, C. F. Burmeister, G. Groenhof, and H. Grubmüller, J. Chem. Phys. **136**, 144304 (2012).

[49] H. I. B. Banks, D. A. Little, J. Tennyson, and A. Emmanouilidou, Phys. Chem. Chem. Phys. **19**, 19794 (2017).

[50] R. Colle and S. Simonucci, Phys. Rev. A **39**, 6247 (1989).

[51] R. Colle and S. Simonucci, Phys. Rev. A **48**, 392 (1993).

[52] R. Colle, D. Embriaco, M. Massini, S. Simonucci, and S. Taioli, J. Phys. B **37**, 1237 (2004).

[53] C. Marante, M. Klinker, I. Corral, J. González-Vázquez, L. Argenti, and F. Martín, J. Chem. Theory Comput. **13**, 499 (2017).

[54] C. Marante, M. Klinker, T. Kjellsson, E. Lindroth, J. González-Vázquez, L. Argenti, and F. Martín, Phys. Rev. A **96**, 022507 (2017).

[55] M. Klinker, C. Marante, L. Argenti, J. González-Vázquez, and F. Martín, Phys. Rev. A **98**, 033413 (2018).

[56] J. V. Ortiz, J. Chem. Phys. **81**, 5873 (1984).

[57] N. Correia, A. Naves de Brito, M. P. Keane, L. Karlsson, S. Svensson, C.-M. Liegener, A. Cesar, and H. Ågren, J. Chem. Phys. **95**, 5187 (1991).

[58] K. Endo, S. Shimada, N. Kato, and T. Ida, J. Mol. Spectrosc. **1122**, 341 (2016).

[59] P. G. Burke, *R-Matrix Theory of Atomic Collisions: Application to Atomic, Molecular and Optical Processes*, Springer Series on Atomic, Optical, and Plasma Physics Vol. 61 (Springer-Verlag, Heidelberg, 2011).

[60] S. I. Bokarev and O. Kühn, Wiley Interdiscip. Rev. Comput. Mol. Sci. e1433 (2019), doi: 10.1002/wcms.1433.

[61] S. I. Bokarev, M. Dantz, E. Suljoti, O. Kühn, and E. F. Aziz, Phys. Rev. Lett. **111**, 083002 (2013).

[62] R. V. Pinjari, M. G. Delcey, M. Guo, M. Odelius, and M. Lundberg, J. Comput. Chem. **37**, 477 (2016).

[63] I. Josefsson, K. Kunnus, S. Schreck, A. Föhlisch, F. de Groot, P. Wernet, and M. Odelius, J. Phys. Chem. Lett. **3**, 3565 (2012).

[64] S. I. Bokarev, M. Khan, M. K. Abdel-Latif, J. Xiao, R. Hilal, S. G. Aziz, E. F. Aziz, and O. Kühn, J. Phys. Chem. C **119**, 19192 (2015).

[65] G. Grell, S. I. Bokarev, B. Winter, R. Seidel, E. F. Aziz, S. G. Aziz, and O. Kühn, J. Chem. Phys. **143**, 074104 (2015).

[66] R. Golnak, S. I. Bokarev, R. Seidel, J. Xiao, G. Grell, K. Atak, I. Unger, S. Thürmer, S. G. Aziz, O. Kühn, B. Winter, and E. F. Aziz, Sci. Rep. **6**, 24659 (2016).

[67] J. Norell, G. Grell, O. Kühn, M. Odelius, and S. I. Bokarev, Phys. Chem. Chem. Phys. **20**, 19916 (2018).

[68] S. Stock, R. Beerwerth, and S. Fritzsche, Phys. Rev. A **95**, 053407 (2017).

[69] A. Kivimäki, S. Heinäsmäki, M. Jurvansuu, S. Alitalo, E. Nõmmiste, H. Aksela, and S. Aksela, J. Electron Spectrosc. Relat. Phenom. **114**, 49 (2001).

[70] H. Yoshida, K. Ueda, N. M. Kabachnik, Y. Shimizu, Y. Senba, Y. Tamenori, H. Ohashi, I. Koyano, I. H. Suzuki, R. Hentges, J. Viefhaus, and U. Becker, J. Phys. B **33**, 4343 (2000).

[71] K. Ueda, M. Kitajima, A. De Fanis, Y. Tamenori, H. Yamaoka, H. Shindo, T. Furuta, T. Tanaka, H. Tanaka, H. Yoshida, R. Sankari, S. Aksela, S. Fritzsche, and N. M. Kabachnik, Phys. Rev. Lett. **90**, 153005 (2003).

[72] Y. Tamenori and I. H. Suzuki, J. Phys. B **47**, 145001 (2014).

[73] J. C. Slater, Phys. Rev. **81**, 385 (1951).

[74] *NIST Handbook of Mathematical Functions*, 1st ed., edited by F. W. J. Olver, D. W. Lozier, R. F. Boisvert, and C. W. Clark (Cambridge University, Cambridge, England, 2010).

[75] P.-O. Löwdin, Phys. Rev. **97**, 1474 (1955).

[76] R. Manne and H. Ågren, Chem. Phys. **93**, 201 (1985).

[77] See Supplemental Material at http://link.aps.org/supplemental/10.1103/PhysRevA.100.042512 for additional results, theoretical details, and the employed basis sets.

[78] F. Aquilante, J. Autschbach, R. K. Carlson, L. F. Chibotaru, M. G. Delcey, L. De Vico, I. F. Galván, N. Ferré, L. M. Frutos, L. Gagliardi, M. Garavelli, A. Giussani, C. E. Hoyer, G. Li Manni, H. Lischka, D. Ma, P. Å. Malmqvist, T. Müller, A. Nenov, M. Olivucci, T. B. Pedersen, D. Peng, F. Plasser, B. Pritchard, M. Reiher, I. Rivalta, I. Schapiro, J. Segarra-Martí,

M. Stenrup, D. G. Truhlar, L. Ungur, A. Valentini, S. Vancoillie, V. Veryazov, V. P. Vysotskiy, O. Weingart, F. Zapata, and R. Lindh, J. Comput. Chem. **37**, 506 (2016).

[79] P.-O. Widmark, P. Å. Malmqvist, and B. O. Roos, Theor. Chim. Acta **77**, 291 (1990).

[80] K. Kaufmann, W. Baumeister, and M. Jungen, J. Phys. B **22**, 2223 (1989).

[81] J. Almlöf and P. R. Taylor, J. Chem. Phys. **86**, 4070 (1987).

[82] I. F. Galván, M. Vacher, A. Alavi, C. Angeli, J. Autschbach, J. J. Bao, S. I. Bokarev, N. A. Bogdanov, R. K. Carlson, L. F. Chibotaru, J. Creutzberg, N. Dattani, M. G. Delcey, S. S. Dong, A. Dreuw, L. Freitag, L. M. Frutos, L. Gagliardi, F. Gendron, A. Giussani, L. González, G. Grell, M. Guo, C. E. Hoyer, M. Johansson, S. Keller, S. Knecht, G. Kovačević, E. Källman, G. Li Manni, M. Lundberg, Y. Ma, S. Mai, J. P. Malhado, P. Å. Malmqvist, P. Marquetand, S. A. Mewes, J. Norell, M. Olivucci, M. Oppel, Q. M. Phung, K. Pierloot, F. Plasser, M. Reiher, A. M. Sand, I. Schapiro, P. Sharma, C. J. Stein, L. K. Sørensen, D. G. Truhlar, M. Ugandi, L. Ungur, A. Valentini, S. Vancoillie, V. Veryazov, O. Weser, P.-O. Widmark, S. Wouters, J. P. Zobel, and R. Lindh, J. Chem. Theory Comput. (2019), doi: 10.1021/acs.jctc.9b00532.

[83] D. Peng and M. Reiher, Theor. Chem. Acc. **131** (2012).

[84] P. Å. Malmqvist, K. Pierloot, A. R. M. Shahi, C. J. Cramer, and L. Gagliardi, J. Chem. Phys. **128**, 204109 (2008).

[85] P. Å. Malmqvist, B. O. Roos, and B. Schimmelpfennig, Chem. Phys. Lett. **357**, 230 (2002).

[86] P. Å. Malmqvist, Int. J. Quantum Chem. **30**, 479 (1986).

[87] Q. Sun, J. Comput. Chem. **36**, 1664 (2015).

[88] T. Hahn, Comput. Phys. Commun. **168**, 78 (2005).

[89] L. Avaldi, G. Dawber, R. Camilloni, G. C. King, M. Roper, M. R. F. Siggel, G. Stefani, M. Zitnik, A. Lisini, and P. Decleva, Phys. Rev. A **51**, 5025 (1995).

[90] T. Möhle, O. S. Bokareva, G. Grell, O. Kühn, and S. I. Bokarev, J. Chem. Theory Comput. **14**, 5870 (2018).